

# A Detailed Thermal Analysis for Performance Improvement of Axial Transverse-flux-switching PM Wind Turbine Generator

A. Ghaehri, *Member, IEEE*, A. Zarghani, *Student Member, IEEE*, E. Afjei, *Senior Member, IEEE*, and H. Torkaman, *Senior Member, IEEE*

**Abstract**—The efficiency of energy conversion from mechanical to electrical in AC generators is not entirely optimal, as power losses are converted into heat. Accurate thermal modeling and temperature measurement of advanced electric machines with complex structures are mandatory to confirm their reliability and safe operation. In a unique axial transverse flux switching permanent magnet (ATFSPM) generator, due to its high power density, large stray loss from leakage flux, compact topology, and totally enclosed structure, thermal analysis is of paramount significance. In this paper, thermal modeling and analysis of ATFSPM are carried out in detail using a three-dimensional (3D) finite element analysis (FEA) to evaluate the thermal condition for a precise performance improvement. To begin, all loss sources are accurately derived using 3-D FEA and analytical methods, taking into account the temperature dependence of material properties, and then losses are coupled to the thermal model as heat sources. Afterward, aiming for realistic thermal modelling, the convection heat transfer in the different regions of internal and external areas as well as thin layers of interface gaps between components are all considered. In addition, the prototype of ATFSPM is supplied to validate the accuracy of 3-D FEA temperature prediction. Furthermore, a novel technique is carried out to effectively improve thermal performance, enhance the efficiency, and limit hot-spot temperatures. The steady-state and transient temperature results demonstrate the high accuracy of the thermal modeling, enhance the secure operation of the ATFSPM, and facilitate increased loading utilizing the proposed technique.

**Index Terms**— Axial flux machine, Efficiency, Flux switching, Loss calculation, Thermal analysis.

## I. INTRODUCTION

**D**IRECT-drive wind turbines (DDWTs) are a type of wind turbine that uses a permanent magnet (PM) generator directly connected to the rotor without the need for a gearbox [1]-[2]. Transverse flux PM (TFPM) machines outperform

other PM counterparts in terms of high value of power density, stator winding simplicity, low winding loss, compact structure, and high pole-pair number at a higher frequency. These prominent advantages offer TFPMs potential candidates for low-speed applications, especially DDWTs, which present higher efficiency, less acoustic noise due to smoother operation, high reliability, and reduced maintenance cost compared to geared ones [3]. By integrating the axial-field structure and flux-switching PM (FSPM) principle of operation, as in the novel configuration of axial transverse FSPM (ATFSPM) [4], it is possible to increase the benefits of TFPMs and achieve full PM utilization, negligible end-windings, as well as simple lamination and manufacturing of the iron cores.

Temperature possesses a negative impact on both electromagnetic and structural performance [5]. PM machines produce considerably more power density than non-PM machines. The energy of PMs is temperature-dependent, as PMs demagnetization occurs at elevated temperatures, resulting in a decrease in torque density [6]. In addition, if the temperature exceeds the critical point, the likelihood of winding insulation and PM coating defects increases, thereby reducing the lifespan [7]. From a mechanical point of view, high temperatures cause difficulties such as thermal fatigue, mechanical pressure on bearings, and alterations in materials texture [8]. For these reasons, overheating causes irreversible damage, necessitating accurate thermal analysis in addition to electromagnetic study for novel configurations.

For the purpose of conducting thermal analysis, lumped parameter thermal network (LPTN) [9]-[11], finite element analysis (FEA), and computational fluid dynamics (CFD) are utilized [12]-[14]. Even though LPTN can be quickly solved, only the average temperature of components can be obtained. CFD is regarded as the most accurate method, but solving 3-D topologies with multiple heat transfer paths requires a significant amount of time and a powerful system processor. Consequently, FEA, which forecasts the temperature distribution with high precision and acceptable process speed, is an appropriate criterion with accuracy similar to experimental tests. Heat generation is an important concern of PMs, particularly FSPM machines, because of a direct contact between the stator core, windings, and PMs as the main heat sources and vulnerable parts. To inquire into this issue, the

Manuscript received January 08, 2025; revised April 03, 2025; accepted May 09, 2025. Date of publication June 25, 2025; Date of current version May 28, 2025.

This work was supported by research grants of the Iran National Science Foundation (INSF) under grant No. 98002866.

A. Ghaehri, A. Zarghani, E. Afjei, and H. Torkaman are with the Department of Electrical Engineering, Shahid Beheshti University, Tehran, Iran. (e-mails: a\_ghaehri@sbu.ac.ir, alizarghani@ieee.org, e-afjei@sbu.ac.ir, h\_torkaman@sbu.ac.ir).

(Corresponding author: a\_ghaehri@sbu.ac.ir)

Digital Object Identifier 10.30941/CESTEMS.2025.00017

steady-state mean temperature in active components of radial-flux FSPMs [15]-[19] and axial-flux FSPM [20] was predicted using FEA and LPTN. Besides, TFPMs suffer from high temperatures, especially in the internal active parts [21] due to the worst heat transfer conditions. In [22] E-cores were implemented instead of U-cores in a TFPM to achieve lower core losses and consequently less heat. In [21], [23] 2-D LPTNs with low accuracy were plotted for TFPM reluctance machines. However, through 3D modeling, the accuracy of LPTN was improved [24]. The 3D thermal FEA in [25] examined temperature distribution in only active components without any detail about heat transfer and loss distribution. In [21], [23]-[25], FEA was used as a validation criterion without providing experimental tests. In [26] thermal FEA of a TFPM with Halbach-Array PMs was presented, and the high temperature of the active components was illustrated.

In order to enhance thermal performance, various solutions have been investigated, including the implementation of cooling systems, the reduction of losses through new materials, and the application of advanced manufacturing techniques. In [27], a forced air-cooled system was developed for a compact DDWT generator, resulting in a reduction of winding and PM temperatures by 11.5 °C and 9.7 °C, respectively. The comparative study results in [28] indicate that water cooling channels improve heat dissipation in air cooling channels within the stator slot, leading to a 47% reduction in winding temperature. Cooling system development introduces challenges related to weight, volume, operational duty, and energy consumption, which are critical for high current density operations [29]-[30]. [31] examined that, while hysteresis and eddy current losses can be reduced through optimal lamination materials, the increase in temperature is limited to only 2 °C. The use of aluminum housing in place of cast iron resulted in a 6% reduction in rotor and housing temperatures for an axial-field FSPM machine [32]. Additive manufacturing (AM) has recently facilitated the design of various winding shapes, resulting in a significant reduction of AC winding losses and a corresponding decrease in winding temperature [33]-[34]. Manufacturing procedures and costs are critical considerations for AM windings, particularly advantageous for high-speed applications. Additionally, AM heat exchangers [35] can be integrated into slots containing concentrated coils to enhance heat dissipation; however, this approach reduces fill-factor and presents assembly challenges for round coils in TFPM topologies. Overall, the most effective approach to mitigate overheating is to identify and eliminate the primary sources of loss, thereby reducing local heat and significantly decreasing the temperature gradient across all components.

The literature states that a number of studies have been conducted on the thermal modelling of TFPMs and FSPMs, but they have not specifically addressed loss reduction or improving thermal performance to achieve appropriate operating conditions. To fulfill this gap, the main purpose of this paper is to investigate the thermal analysis of an ATFSPM generator and propose a new technique with the aim of stray loss suppression to reach a higher torque density and

efficiency. In ATFSPM, as a consequence of the 3D magnetic circuit, passive components experience significant flux leakage. Also, heat dissipation to the ambient is poor due to the compact and entirely enclosed construction, resulting in a high interior temperature. Such problems require complex multi-physics 3-D FEA to investigate the actual ATFSPM performance. Hence, the losses in all the active and passive components are extracted using 3-D FEA in the time domain, and a precise thermal modeling is developed to approximate the temperature distribution with mesh-to-mesh direct loss mapping in a bidirectional magneto-thermal coupling, which is then confirmed by experimental measurement. Furthermore, a new approach based on utilizing carbon-fiber material for the rotor carrier is adopted to reduce hot-spot temperature and PM demagnetization risk. The main contribution of this paper can be summarized as follows:

- 1) Accurate calculation of losses, considering the temperature dependency of material properties, using 3D time-stepping transient finite element modeling, validated by experimental results.
- 2) Development of a precise thermal circuit that incorporates both active and passive components, along with an accurate evaluation of all thermal mechanisms.
- 3) Implementation of a two-way magneto-thermal analysis to capture the interaction between temperature rise and magnetic performance.
- 4) Experimental validation through direct measurement of losses and component temperatures in an axial-transverse-flux-switching PM generator.
- 5) Introduction of a novel passive cooling technique using a carbon-fiber rotor carrier, which effectively enhances efficiency and power factor, significantly reduces power losses, and limits hot-spot formation.

The rest of the paper is organized as follows: The topology and operating principle of ATFSPM are introduced in Section II. In Section III, the process of electromagnetic-thermal coupled analyses is presented, considering the temperature dependency of material properties. Section IV is dedicated to the thermal modeling, in which various heat transfer paths and heat transfer coefficients are examined and calculated in the thermal network. Finally, thermal analysis by 3-D FEA and the experimental test are conducted, and an approach will be adopted to improve efficiency and thermal performance in Section V.

## II. ATFSPM STRUCTURE

Based on the literature, almost all direct-drive PM wind turbine generators fall into the category of small-scale vertical-axis generators. Hence, the selection of an appropriate working point for generators is crucial. The nominal speed and power of ATFSPM generators are selected according to [26]. The 3D exploded view and constructed components of the compact ATFSPM are depicted in Fig. 1. As can be seen, this construction has a double-sided configuration and is composed of I-shaped segmented rotors and a single H-shaped segmented stator, all of which are laminated in a circumferential direction.

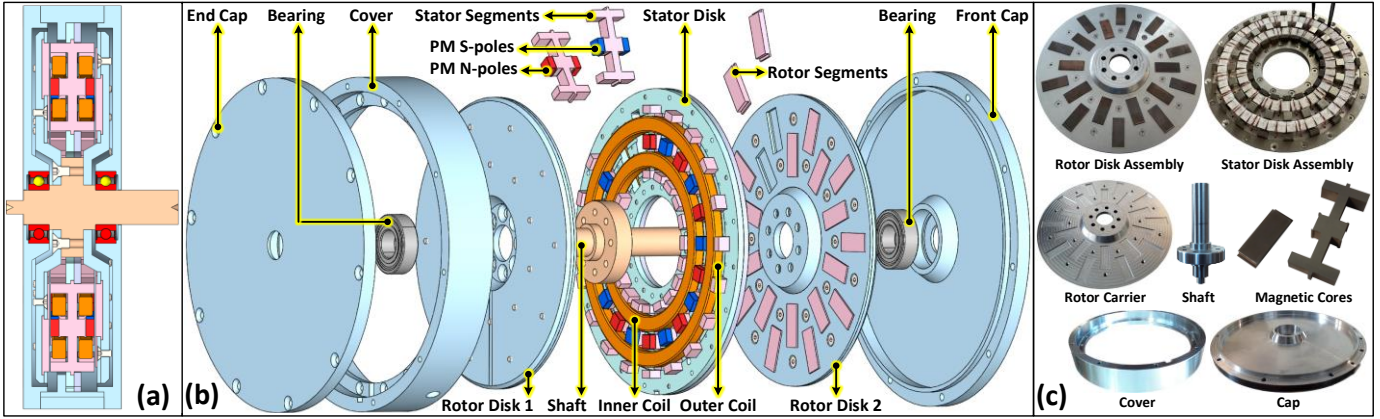


Fig. 1. Compact ATFSPM generator. (a) Cross-section view. (b) 3-D exploded view. (c) Parts and assemblies.

The flux-switching principle is created by adhering axially magnetized PMs to the middle layer of each stator pole, where the magnetization direction of PMs on each pole is opposed to one another, as depicted in Fig. 2. One of the TFPM's benefits is the absence of electromagnetic connections between phases. For this reason, only one phase of ATFSPM needs to be modeled for performance prediction. In the ATFSPM, four series ring-coils, forming the phase winding, surround the PMs in the stator's slots. The inner and outer coils are located to form a short flux path with minimum core losses along with full utilization of the expensive rare-earth PM. In order to retain the stator poles in position, a holder is employed that is attached to the cover.

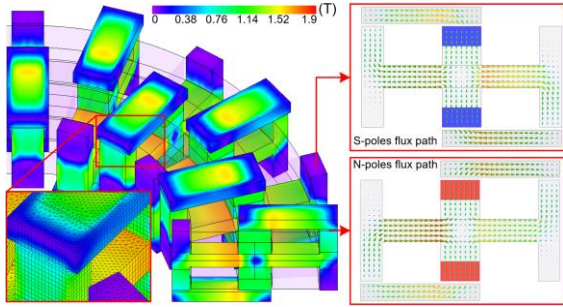


Fig. 2. Magnetic flux density distribution and flux path in the ATFSPM at the phase maximum linkage flux position.

TABLE I  
RATED VALUE AND MAIN DIMENSIONS OF THE ATFSPM

Parameter	Quantity
Rated power/W	325
Rated current/A	5
Current density/(A/mm <sup>2</sup> )	4.5
Pole number	20
Rated speed/rpm	600
Air-gap length/mm	0.7
Turns per phase	400
Outer diameter/mm	191.5
Inner diameter/mm	89.1
Active stack length/mm	35.65
PM remanent flux/T	1.31
Insulation class	H

To further protect the rotor segments and maintain them in

place, carriers are utilized. Finally, two caps are fastened to the cover to form the frame. One of the promising benefits of the ATFSPM is electrically and magnetically decoupled phases. Hence, by assembling similar single-phase machines in proper mechanical phase difference, a multi-phase machine can be achieved. The main concept and operation principle of the ATFSPM are presented in [4]. Table I states the specifications of the ATFSPM. In the following, the process of magneto-thermal analyses is described, and losses are extracted.

### III. COMPREHENSIVE LOSS ANALYSIS

Power losses cause heat generation and a rise in temperature, which subsequently degrades overall machine performance. Hence, accurate identification and calculation of power losses are essential. Owing to the complex 3D magnetic field of ATFSPM, the leakage flux is excessive, and the flux path pattern is constantly changing with time, so that high stray loss will occur in both active and passive components. Besides, the temperature dependence of electromagnetic performance, notably torque density, is a result of the fact that the characteristics of materials change with temperature. Therefore, accurate calculation of losses by considering the temperature effect on materials' properties is another issue to achieve acceptable analysis. Fig. 3 represents the steps involved in conducting the magneto-thermal study. The magnetic analysis starts with ATFSPM design with dimensional parameters and continues by applying nominal conditions and load specifications. Next, in an automatic iterative process, the losses of all components are accurately calculated in a real-time manner. So that the effect of losses on electromagnetic performance can be observed while the materials' properties are updated until the component's temperature reaches a steady state. It should be noted that winding resistance is calculated analytically at critical temperature, and also in the first step of 3-D FEA, the material's properties are considered at the ambient temperature of 20 °C ( $T_a$ ). Then, losses in all components are calculated in the time domain and coupled directly to the same component with the same mesh quality in the thermal analysis as the heat sources.

TABLE II  
 THERMAL PROPERTIES OF THE COMPONENTS' MATERIAL

Component	Material type	Thermal conductivity (W/m/°C)	Density (kg/m <sup>3</sup> )
Winding	Copper	400	8960
Stator & Rotor core	ES 50A470	27.8	7700
PMs	NdFeB N42SH	7.6	7500
Carrier & Frame	Aluminum 7075-T6	130	2810
Stator holder	Aluminum 6061-T6	167	2700
Shaft	Steel S45C	46.6	7800
PM adhesive	Loctite 638	0.22	1100
Winding insulation	Nomex 414	0.139	1120
Interface gap	Air	0.025	1.184

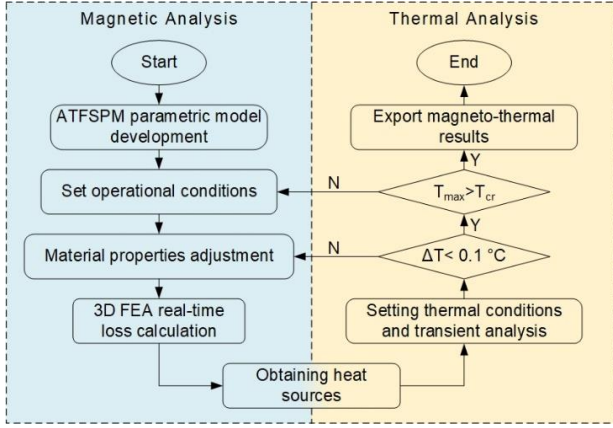


Fig. 3. The flowchart of electromagnetic-thermal analysis.

In the thermal field study, heat transfer boundary conditions are established, and then both transient and steady-state temperatures are obtained. As long as the difference between the newly calculated temperature and the previous temperature ( $\Delta T$ ) is greater than  $0.1^\circ\text{C}$ , the new temperature is considered for the materials' thermal properties and component resistance. After reaching the steady temperature, the maximum temperature ( $T_{\max}$ ) of ATFSPM in different parts is evaluated; if it exceeds the critical temperature ( $T_{\text{cr}}$ ), e.g.,  $140^\circ\text{C}$  for PM, it is necessary to set the new operating conditions, which cause the performance degradation. In this case, this paper presents an innovative technique in Section V. Table II lists the thermal properties of the materials utilized in the ATFSPM. It should be mentioned that due to core lamination, thermal conductivity in the in-plane direction is less than in other directions. In the following, the losses of all components of the ATFSPM are extracted.

#### A. Copper Loss

The primary heat source is copper loss, which is directly proportional to the armature current and phase resistance. The temperature dependency of resistance is a missing item in most investigations. Winding eddy-current loss of ATFSPM is negligible due to thin-diameter, highly distributed coils. The copper loss can be written as:

$$P_c = R_c \left[ 1 + \alpha_T (T_c - T_a) \right] I_{\text{rms}}^2 \quad (1)$$

where  $R_c$  ( $\Omega$ ),  $\alpha_T$ ,  $T_c$  ( $^\circ\text{C}$ ),  $T_a$  ( $^\circ\text{C}$ ), and  $I_{\text{rms}}$  (A) are phase resistance, copper temperature coefficient (0.393% per  $^\circ\text{C}$ ), coil temperature, ambient temperature, and RMS value of

armature current, respectively. As a practical result, the phase resistance at  $140^\circ\text{C}$  is increased by about 47% compared to the ambient temperature of  $20^\circ\text{C}$ . Phase resistance of the inner and outer coils in the actual condition can be calculated as follows:

$$R_{\text{ci}} = \frac{4k_{\text{ca}}\rho_k N_c}{D_w^2} (D_g - H_{\text{pm}} - H_{\text{ss}}) \quad (2)$$

$$R_{\text{co}} = \frac{4k_{\text{ca}}\rho_k N_c}{D_w^2} (D_g + H_{\text{pm}} - H_{\text{ss}}) \quad (3)$$

where  $\rho_k$  is pure copper specific resistance ( $1.68 \times 10^{-8}$ ),  $N_c$  is turns number per coil,  $D_w$  is wire diameter,  $D_g$  is the air-gap diameter,  $H_{\text{pm}}$  is the height of PM, and  $H_{\text{ss}}$  is the height of the stator segment. Also,  $k_{\text{ca}}$  is the coefficient of copper alloy, which was not considered in the prior research despite its intense influence (1.2-1.3 for general magnet wire). Likewise, the copper loss of the inner coils and outer coils is 35.44 W and 50.86 W, respectively. It is important to mention that the high-frequency ohmic losses are neglected due to low angular velocity. However, considering  $k_{\text{ca}}$  in (2)-(3) covers this type of loss.

#### B. Electromagnetic Losses

In TFPM machines, the  $x$ ,  $y$ , and  $z$  components of flux density cause electromagnetic losses, resulting in energy losses in the lamination and in-plane directions. The conventional method of calculating core losses [20], [26] is less precise because a fast Fourier transform post-processed equation is applied to the magnetic flux density waveform of each element based on the magnetic loss table of the material producer datasheet. Electrical steel sheet producers present the loss table values according to only the  $x$ - $y$  component of the flux density. In TFPMs, there is a huge  $z$ -component of flux density, which will cause a considerable iron loss in the in-plane direction. Despite the prior literature, this paper utilizes a simultaneous-processing method within the magnetic study instead of a post-processing method to determine iron losses precisely. Variations of the PM working point with time produce eddy currents in well-conductive rare-earth materials. Due to the temperature-dependent resistance of PMs, we must consider the temperature correction factor when examining the PM eddy-current loss. Fig. 4 shows that the front surfaces near the air gap have higher eddy current loss than the back surfaces attached to the stator segment. This is because the flux changes more in the front.

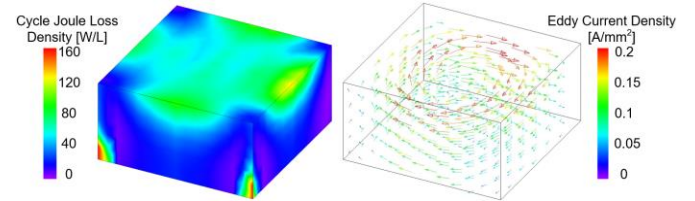


Fig. 4. Loss density and current density in PM.

Fig. 5 illustrates the iron loss density distribution in the rotor and stator segments, where rotor loss density is larger than stator modules. The loss density of faces towards the air gap has experienced a higher value. Although the rotor

rotation causes the severe flux variation in the side teeth of the stator segments, the middle section of the stator segments has negligible flux variation and much lower losses due to the stability of the magnetic flux density created by the PMs.

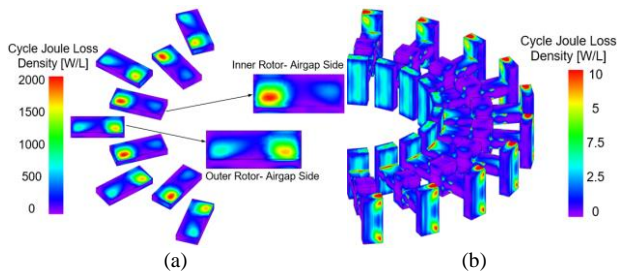


Fig. 5. Loss density distribution. (a) I-shaped rotor segments. (b) H-shaped stator modules.

Fig. 6(a) manifests that heavy eddy current loss is generated in the carrier due to large magnetic flux leakage variations of passive rotor segments. It is clear that the eddy currents within the carrier have closed their path from the regions between the rotor segments, where nearly significant losses were formed. According to Fig. 6(b), a portion of the unwanted carrier flux leaks into the caps, resulting in a distribution of eddy losses that is identical to the carrier loss with a smaller amount. Fig. 6(c) indicates the stator holder experiences a low loss density due to its significant distance from the center of flux variations and the fact that the PMs of ATFPM are located in the stator so that an appropriate flux stability leads to a lower alternative flux leakage.

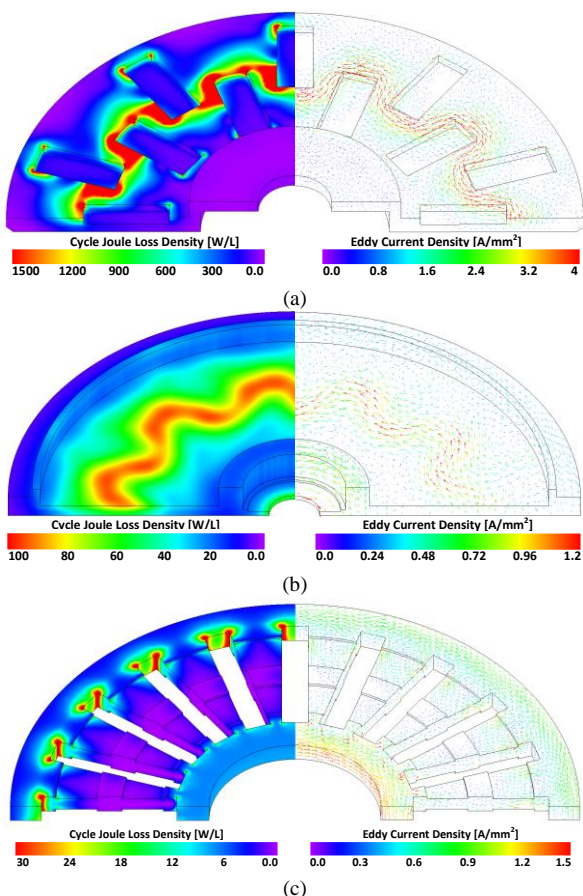


Fig. 6. Eddy-current and loss density. (a) Carrier. (b) Cap. (c) Holder.

It should be noted that the eddy current loss in the cover is negligible due to low stray magnetic flux; however, it affects the heat dissipation, as is explained in the next section. It is worth mentioning that the derived value of losses for passive components is considered temperature-dependent, as their electrical resistances vary with temperature.

C. Experimental Evaluation

The test setup of Fig. 7(a) is provided to validate the electromagnetic performance as well as the total loss quantities of the constructed ATFSPM. The prime mover, an induction motor, operates under the control of a VFD driver to meet the requirements of the ATFSPM generator, e.g., 600 rpm. The ATFSPM generator is coupled to the nominal ohmic load via a grounded star configuration. In Figs. 7(b)-(c), we can see that the highest values for voltage and current at full load in both the 3-D FEA simulation and test results are nearly the same, at 130 V and 5 A. The power analyzer measures the electrical output power, while a torque-speed transducer measures the actual mechanical input power. It is noteworthy that the voltage curve that is shown in Fig. 7(a) is related to the open-circuit voltage, which is used to validate the conformity of simulations by the manufactured ATFSPM generator, which was fully investigated by the authors in [4].

Table III compares the losses of ATFSPM’s components by 3-D FEA and experimental measurement at the nominal condition. The high degree of agreement between the results of the 3-D FEA and the experimental test can be attributed to the meticulous consideration of the temperature-dependent properties of the materials as well as the comprehensive calculation of losses in the time domain. However, 3-D FEA forecasts are marginally as much as 0.9% lower than the experimental findings because the FEA does not take into account the impacts of the manufacturing errors and materials property uncertainties.

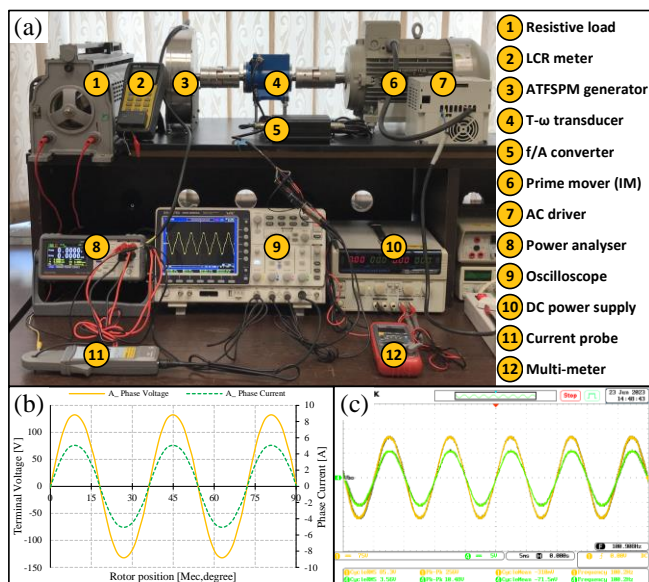


Fig. 7. Experimental test setup and voltage/current waveforms in nominal load. (a) ATFSPM test setup. (b) Simulation. (c) Measured.

TABLE III  
 POWER LOSSES OF EACH COMPONENT OF THE ATFSPM

Type	Component	3-D FEA (W)	Experimental (W)
Joule loss	Inner coils	35.44	36.26
	Outer coils	50.86	
	PMs	0.4	
Iron loss	Rotor	11.8	105.3
	Stator	0.82	
Stray loss	Carrier	66.9	193.3
	Holder	5.9	
	Cover	4.48	
	Caps	14.9	
Total loss		191.5	193.3

It can be concluded that an extremely large stray loss of carriers in the ATFSPM causes a drop in power factor, efficiency, and thermal issues, necessitating a proposal of an approach to reduce the carrier loss. The calculated losses are considered as heat sources in the thermal analysis.

#### IV. 3D THERMAL MODELLING

Thermal modeling requires the identification of heat transfer paths in various areas and the design of the thermal network, followed by the computation of heat transfer elements. In this section, all convection boundary conditions are described in detail, along with interface gaps in the contact surfaces of different components.

##### A. Thermal Network

The thermal network of the ATFSPM is presented in Fig. 8, which describes how heat is transferred between various parts. It should be noted that, for the sake of simplicity, a 2D cross-section of the thermal network is depicted, whereas the thermal network has actually been constructed and modelled in three dimensions, i.e., radial, axial, and circumferential. As can be seen, in order to represent heat transfer by conduction, the stator set (stator segments, coils, PMs, and stator holder), rotating elements (rotor segments, carrier, and shaft), as well as the frame (consisting of cover and caps), are in contact with their respective components via contact resistances. Besides, heat dissipation through convection is separated into external and internal regions. In order to accurately estimate the complex fluid dynamics inside the ATFSPM, the internal air is divided into several regions, including the air-gap, upper end-space, bottom end-space, and carrier rear region (which is a trapped air between the carrier and cap). These regions are linked together via convection resistances, which express fluid circulation within the generator. Similarly, further convection resistances are used to connect adjacent component surfaces to the aforementioned internal air regions. Furthermore, external convection is characterized by thermal convection resistances of the exterior surfaces of the cover, end-caps, and shaft to the ambient. It is essential to note that each component is subjected to a 3-D conductive heat transfer that is considered according to the specific dimensions and the material's thermal properties.

##### B. Thermal Contact Resistances

Thermal contacts are imperfections in the connections between two distinct components that lead to heat leakage and diminish the effect of heat transfer. The contact resistance can be determined by applying the expression below and assuming a very thin layer of air or adhesive between the parts.

$$R_c = \frac{L_c}{k_a A_c} \quad (4)$$

where  $k_a$  is the thermal conductivity of interface material,  $A_c$  ( $m^2$ ) is contact area, and  $L_c$  (m) is imperfection gap depends on the adjacent materials hardness and the pressure applied to the parts. The imperfection gaps [36] between various parts that are joint to each other are listed in the Table IV.

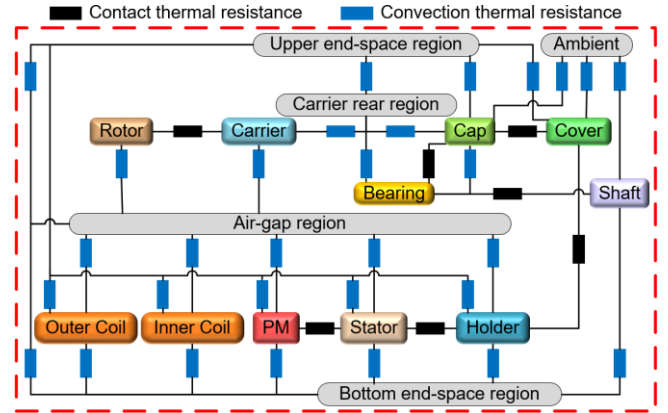


Fig. 8. Thermal network schematic of the ATFSPM.

 TABLE IV  
 INTERFACE GAPS BETWEEN VARIOUS COMPONENT OF THE ATFSPM

Components in contact	Effective gap (mm)
Stator - PM	0.007
Stator - holder	0.01
Holder - cover	0.005
Rotor - carrier	0.01
Cover - cap	0.005
Carrier - shaft	0.0073
Bearing - shaft	0.0112
Bearing - caps	0.0112
Bearing equivalent gap	0.16

##### C. Convection Heat Transfer Resistances

The computation of convection coefficients is the most challenging step of a precise thermal analysis because they are a complex function of the velocity and dynamic properties of the fluid. By solving the equations based on Newton's laws, the convection resistance is obtained as follows:

$$R_v = \frac{1}{h_v A_v} \quad (5)$$

where  $h_v$  ( $W/m^2/^\circ C$ ) and  $A_v$  ( $m^2$ ) are the thermal convection coefficient (which must be calculated according to the Nusselt number) and the surface on which the heat dissipates. Heat transfer coefficients of all components that are in contact with the internal and external fluids are considered and need to be calculated appropriately based on specific correlations, which are described in the following. It is worth mentioning that, as

no cooling system is developed for the ATFSPM, the natural convection is assumed for all regions. Although the rotor-stator system in axial flux machines acts as an axial fan [37], considering the natural convection is reasonable for ATFSPM due to its low operational speed.

### 1) Air-gap and Carrier Rear Regions

The internal fluid dynamics of the axial and radial flux structures are different, which makes employing the convection coefficient correlations associated with axial flux machines crucial. So, dimensionless rotational Reynolds number and gap ratio are expressed by:

$$Re_{\theta} = \frac{\Omega R^2}{\varrho} \quad (6)$$

$$G = \frac{l_g}{R} \quad (7)$$

where  $\Omega$  (rps) is the rotational speed,  $R$  (m) is the disk radius,  $\varrho$  is the fluid kinematic viscosity, and  $l_g$  (m) is the gap length. Based on the values of  $Re_{\theta}$  and  $G$ , four different regimes investigated in [38]. According to the structural dimensions of the ATFSPM, the fluid flow is laminar, and the Nusselt number is obtained via the equation below:

$$Nu = 7.46Re_{\theta}^{0.32} \quad (8)$$

### 2) End-space Areas

To describe the heat transfer rate from the radial peripheral face of rotational components, Reynolds and Nusselt numbers are derived as [39]:

$$Re_D = \frac{\Omega D^2}{\varrho} \quad (9)$$

$$Nu = 0.133 \frac{Re_D^{2/3}}{4} Pr^{1/3} \quad (10)$$

where  $D$  (m) and  $Pr$  are the components' diameter and air Prandtl number which is 0.7323. Besides, Nusselt number for the radial surface of the stationary components in laminar regime is developed as [40]:

$$Nu = 0.35Re_{\theta}^{0.5} \quad (11)$$

### 3) External Surfaces

Heat transfer in static components can be separated into two parts: a cylinder for the radial surface of the cover and a disk for the axial surface of the caps. Grashof and Nusselt numbers for cylinder ( $Nu_c$ ) and disk ( $Nu_d$ ) are derived using below correlations [41]:

$$Gr = \frac{\beta g R^3 \pi^{3/2} \Delta T}{\varrho^2} \quad (12)$$

$$Nu_c = 0.525(GrPr)^{0.25} \quad (13)$$

$$Nu_d = 0.59(GrPr)^{0.25} \quad (14)$$

Here,  $\beta$  is the coefficient of thermal expansion ( $1/^\circ\text{C}$ ),  $g$  is acceleration of gravity ( $\text{m/s}^2$ ), and  $\Delta T$  is the temperature difference between the component surface and the ambient.

In regards to rotational components, the heat transfer correlation of Reynolds number and Nusselt number for the radial periphery ( $Nu_r$ ) and axial surface ( $Nu_a$ ) is as follows [42]:

$$Nu_r = 0.133Re_D^{2/3} Pr^{1/3} \quad (15)$$

$$Nu_a = 0.119Re_{\theta}^{2/3} \quad (16)$$

where  $Re_D$  is Reynolds number in radial peripheral faces. In accordance with the abovementioned analytical equations, Table V states the calculated heat transfer coefficients.

TABLE V  
AVERAGE HEAT TRANSFER COEFFICIENTS

Area	Coefficient ( $\text{W/m}^2/^\circ\text{C}$ )
Rotor, stator, PMs, coils, and holder to air-gap	57.2
Carrier to air-gap	55.8
Stator, coils, holder, and cover to upper end-space	17.9
Carrier to upper end-space	45.8
Stator, coils, and holder to bottom end-space	17.9
PM and Carrier to bottom end-space	32.8
Shaft to bottom end-space	30.1
Cap and carrier to carrier rear region	55.8
Bearing to carrier rear region	98.8
Cover to ambient	11
Caps to ambient	14.4
Radial surface of the shaft to ambient	36.7
Axial surface of the shaft to ambient	15.3

## V. THERMAL ANALYSIS

In this section, thermal analysis by 3-D FEA is conducted, and temperature distribution in all components as well as heat flow paths are demonstrated. Afterward, the experimental evaluation is performed to validate the accuracy of 3D thermal network and simulations. Finally, a distinctive technique is proposed to improve the thermal performance of ATFSPM.

### A. 3-D FEA

To perform accurate thermal analysis at nominal conditions, power losses of the components are directly coupled to each generated mesh element in order to achieve a distributed heat generation. 3-D FEA thermal analysis with the equivalent thermal circuit based on Fig. 8 has been conducted in JMAG-designer software. The temperature distribution of all components when ATFSPM reaches a steady-state condition is demonstrated in Fig. 9. As can be observed, the exterior surfaces, which are exposed to the ambient air and have fewer losses, experience a lower temperature compared to the internal components. Fig. 9(a) reveals that the edge of the cover that is connected to the stator holder has a higher temperature than other areas because heat penetrates the joint area and is dissipated from the rest of the surfaces. Since heat is transferred from the carrier to the PMs through the air-gap, Fig. 9(b) exhibits that the surface of the PM facing the air-gap is warmer by  $0.7^\circ\text{C}$  compared to the stator side. Fig. 9(c) shows that although inner windings created less copper loss than outer windings, they experienced a greater temperature up to  $3^\circ\text{C}$  as a result of significant loss density in the inner regions of components as well as difficult heat dissipation. It is also clear that the maximum temperature of the windings is  $136^\circ\text{C}$ , which is lower than the critical temperature of the insulation material ( $180^\circ\text{C}$ ). In addition, Fig. 9(d) indicates

how the high temperature of the inner coil causes the inside surface of the holder to become hotter than its outer surface, where the heat is transferred to the cover and finally to the outside air. As Fig. 9(e) manifests, the hotspot with a temperature of 144 °C is located in the carrier and rotor segments due to a substantial amount of stray loss in the carriers. Comparing Fig. 9(d) and Fig. 9(f) reveals that, owing to the direct connection between the stator segments and stator holder, these components are almost at the same temperature distribution. As previously shown in Fig. 5(a), the loss density in the inner radius of the stator segment was high, and it can be seen carefully in Fig. 9(f) that these regions are hotter because of more heat production and poor heat dissipation.

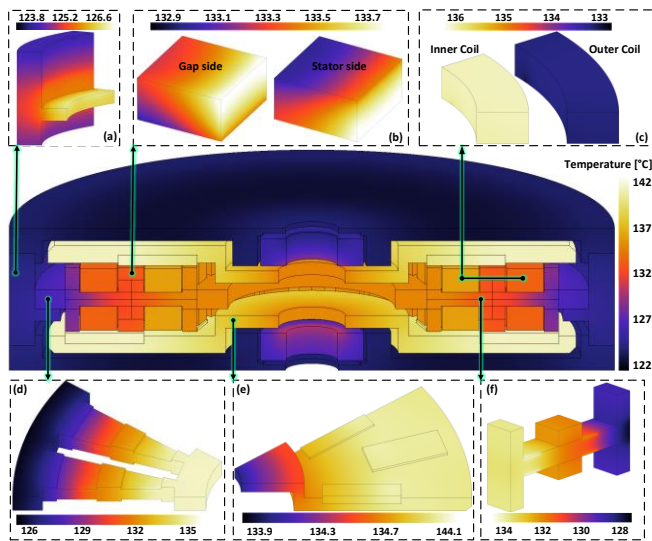


Fig. 9. Temperature distribution. (a) Cover. (b) PM. (c) Coils. (d) Stator holder. (e) Carrier and rotor segments. (f) Stator segment.

For a more detailed evaluation of the thermal aspect, the heat flux path of the ATFSPM is plotted in Fig. 10. Heat is transferred through the air-gap region from the carriers, which is the hot spot, to the stationary parts with lower temperatures. Also, some of the carriers' heat is dissipated through the rear surfaces of the carriers to the caps and then to the ambient. As well, a substantial portion of the heat in the carriers is transferred to the shaft, which is the rotating component (with the lowest temperature), and then flows to the ambient environment. Furthermore, a small amount of heat is transferred to the surrounding air by conduction between the stator cover and holder, which are coupled to one another. Due to the dominant loss of carriers, a huge amount of heat flux enters the PMs, which may lead to permanent demagnetization. This problem is resolved in the final part.

**B. Experimental Verification**

The experimental test is conducted under nominal load conditions until the ATFSPM reaches its steady-state temperature. KTY84-type thermistors are utilized for the purpose of temperature measurement. In accordance with Fig. 11, one sensor is installed within the inner coil and another within the outer coil, and the average temperature of the sensors is chosen as the measured result. Meanwhile, two

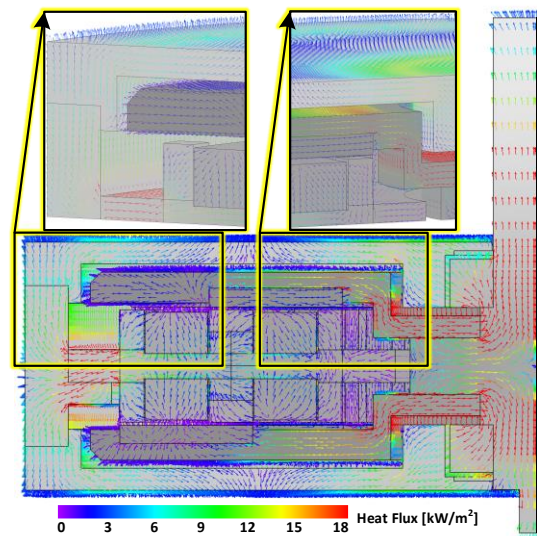


Fig. 10. Heat flux vectors distribution.

additional sensors are installed on the cover and the inner radius of the end-cap to approximate the bearing temperature. The transient temperature is recorded every 5 mins until the steady-state thermal condition is reached after 120 mins.

The experimental validation was carried out using a carefully designed setup involving precise instrumentation to measure mechanical losses and thermal performance under various operational conditions. Key challenges included ensuring accurate placement of thermal sensors and minimizing misalignment of rotating components, both critical for validating the thermal model and the overall efficiency of the generator. The load conditions were also challenging, as temperature rise in the generator required manual adjustment of the applied load to account for changing losses. The uncertainty in the measurements was estimated to be around 5%, considering potential sources of error such as sensor calibration and environmental conditions. Repeatability was ensured by controlling experimental conditions and aligning the setup as closely as possible for each test. Calibration of all devices was performed according to industry standards, and future research will focus on automating load adjustments for improved accuracy and repeatability.

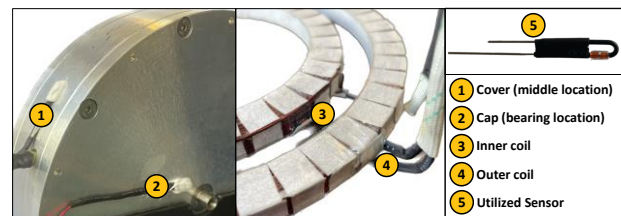


Fig. 11. Installed sensors in various parts of ATFSPM.

According to Fig. 12, the temperature of different components has increased gradually from the initial temperature of 20 °C until reaching steady-state after 2 hours of operation. It is evident that the various components' temperature rise is within the proper range, which validates the simulation results. The average temperature value of different components determined by 3-D FEA and experimental measurement is compared in Table VI. The

maximum error for windings is 1.4 °C, indicating that the 3-D FEA predicted the temperature with an acceptable relative error of less than 1.1%. However, the bearing error is greater than 2.2 °C due to the fact that the relevant sensor was mounted in an external region where the surrounding environment reduced its temperature. It should be noted that the location and installation method of the temperature sensors have a significant impact on the measurements. Accordingly, the defined probes in the simulations are in full compliance with the installation location of the temperature sensors installed on the generator. Also, in order to ensure accurate measurement, a special adhesive with a high heat transfer coefficient has been used to minimize the environmental effect on the sensor, especially in the sensors that are installed outside of the generator, in which one side of them is on the generator and their other side is exposed to the ambient. To improve the condition, a slight indentation should be created in the location where the sensors are installed. Moreover, the uncertainty in measurement and data reading could make a significant error. However, by choosing the proper type of sensor and utilizing accurate loggers with shielded wiring, this error is reduced as much as possible. The results comparison proves the high accuracy of the developed thermal model of the ATFSPM due to its accurate thermal network, careful consideration of all boundary conditions, and precise calculation of thermal circuit elements.

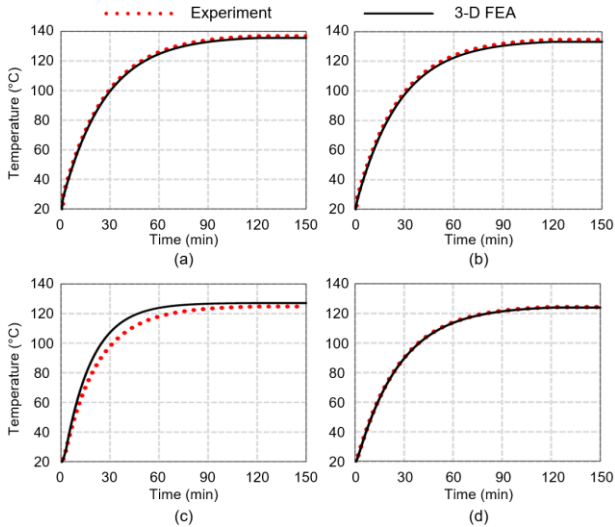


Fig. 12. Transient temperature result comparison. (a) Inner coil. (b) Outer coil. (c) Bearing. (d) Cover.

TABLE VI  
COMPARISON BETWEEN AVERAGE TEMPERATURES 3-D FEA AND MEASURED

Component	3-D FEA	Experimental	Error (%)
Inner coil	135.6	136.8	-0.88
Outer coil	133.1	134.5	-1.04
Bearing	127.1	124.9	1.76
Cover	123.8	124.2	-0.32
Stator segments	132	-	-
Carrier	140	-	-
PM	133.2	-	-
Shaft	127.6	-	-
Cap	123.7	-	-

Considering material temperature dependency allowed exact heat source loss computation. It could be concluded that the windings and PMs suffered from high temperatures. Thus, it is essential to deliberate actions to improve the thermal condition, which are discussed in the following.

### C. Thermal Performance Improvement

As concluded, excessive carrier loss caused a peak temperature of more than 140 °C and, as a result, a drop in overall efficiency. Since the hot spot is located in the rotating components and the windings are located in the enclosed space between the stator segments, utilizing a cooling system to reduce the temperature is complicated and less effective. Therefore, employing a simple and advantageous solution is required to improve the thermal performance of the ATFSPM. Reducing losses is the most effective method for decreasing the hotspot temperature. In this case, the optimal solution is to reduce or eliminate the losses of the components that are not part of the active magnetic circuit but have suffered immense losses. Therefore, altering the carrier's material with a high-resistive and rigid composition is efficient. As a substitute for aluminum, carbon-fiber is extremely desirable due to its high tensile strength, low mass density, and low electrical conductivity. However, the lower thermal conductivity of carbon-fiber composition leads to inadequate heat dissipation from the carrier, necessitating an examination of its influence on the overall magnetic and thermal performance. Thus, its impact on the carrier loss and the temperature distribution is analyzed. By adopting the magnetic and thermal properties of carbon-fiber [43], the temperature distribution and the heat flux path in different components are presented in Fig. 13. As can be noticed, the hot-spot is transferred to the windings, and the maximum temperature is decreased by 33 °C. Also, in this condition, the heat flux path pattern has changed so that the heat of the windings is transferred to the carrier through the air-gap and exits through the carrier rear region to the end caps and subsequently to the ambient. In addition, PMs have experienced appropriate thermal conditions. Fig. 14 depicts a comparison between the carbon-fiber and aluminum carriers in terms of temperature, loss, and efficiency. It is evident that by adopting a carbon-fiber carrier, the eddy loss has been drastically reduced from 66.9 W to 0.53 W, resulting in a 12.2% increase in efficiency. Moreover, considering the eddy loss reduction of carbon-fiber carrier and its effect on the leakage flux as well as the corresponding negative reaction on the power factor, in addition to the efficiency enhancement, the power factor of the ATFSPM generator experienced an increase of 8 % to 0.82 compared to the reported value in [4]. It is worth noting that although the carbon-fiber material has improved the overall performance of the generator, the manufacturing cost is an important key parameter that is investigated and compared to the aluminum counterpart. Table VII summarizes the abovementioned comparison results of the two generators.

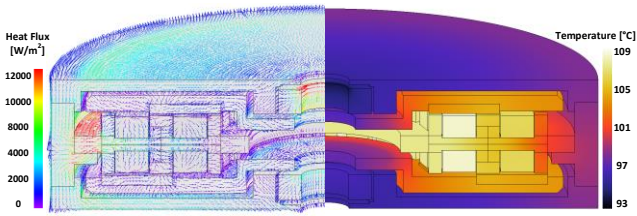


Fig. 13. Temperature distribution and heat flow path of improved ATFSPM.

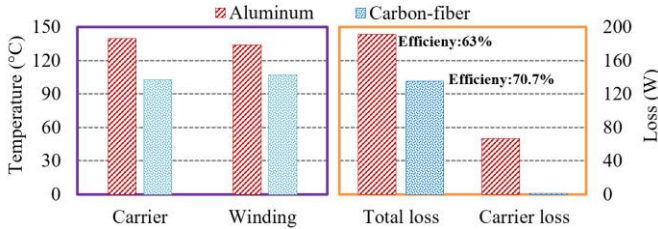


Fig. 14. Loss and efficiency comparison based on the carrier material.

TABLE VII

PERFORMANCE COMPARISON OF THE INITIAL AND IMPROVED ATFSPM

Item	Initial ATFSPM	Improved ATFSPM	Improvement (%)
Carrier loss/W	66.9	0.53	99.2
Total loss/W	191.5	135.1	29.4
Efficiency/(%)	63	70.7	12.2
Power factor	0.76	0.82	7.9
PM temperature/( °C)	133.1	105.7	20.6
Winding temperature/( °C)	134.4	107.2	20.2
Carrier temperature/( °C)	140	103	26.4
Carrier weight/kg	1.084	0.707	34.8
Carrier manufacturing cost (per unit)	1	1.47	-47

To assess the carrier’s mechanical integrity, displacement and stress distribution in carriers formed from carbon fiber and aluminum are evaluated under identical conditions. The electromagnetic forces resulting from the transient magnetic study under nominal load are mapped onto the structural analysis using 3-D FEA. Meanwhile, the carrier endures mechanical stress and deformation as a result of centrifugal and electromagnetic forces. The displacement study in Fig. 15(a)-(b) shows that the carbon-fiber carrier has much lower deformation than aluminum, indicating higher structural stiffness. The greatest displacement in the aluminum carrier is roughly 32 micrometers; nevertheless, the carbon-fiber carrier has half the value of aluminum, improving its dimensional stability. Besides, most of the radial displacement is caused by the mechanical tension from the axial rotation. Moreover, the stator and rotor interact electromagnetically, which contributes to the deformation. Using von Mises stress contours in Fig. 15(c)-(d), it is clear that the most stress occurred close to the carrier’s inner edge, where mechanical loads are largest. Furthermore, the comparison reveals that carbon-fiber and aluminum carriers are not subject to yield or fracture. As a result, it can be stated that the carbon-fiber carrier has significantly lower displacement and a favorable stress distribution, demonstrating its acceptable mechanical stability for use as an alternative to aluminum as the carrier material for the multi-physics performance improvement of

the ATFSPM generator.

As can be concluded, this paper demonstrated that utilizing carbon-fiber material effectively enhances thermal performance without the need for additional cooling components such as pumps, pipes, nozzles, or heat exchangers. Moreover, this approach improves reliability and reduces overall system weight, making it a promising alternative to conventional advanced cooling systems.

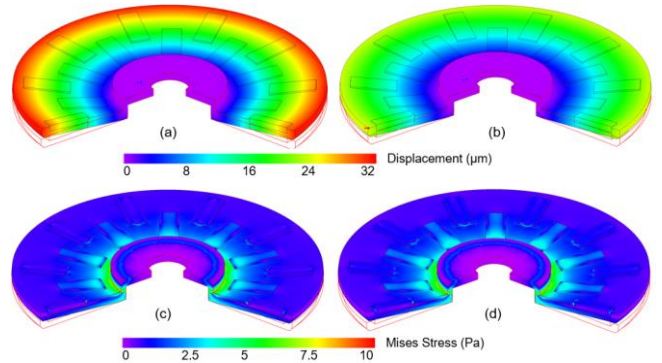


Fig. 15. Carrier displacement and mises stress in scale factor of 2500. (a) Aluminum displacement. (b) Carbon-fiber displacement. (c) Aluminum stress. (d) Carbon-fiber stress.

The adoption of the proposed carbon-fiber rotor carrier solution is expected to have significant long-term benefits for the industrial sector. While carbon-fiber materials incur higher initial manufacturing costs, advancements in manufacturing techniques such as automated fiber placement and resin transfer molding are helping to reduce these costs. The scalability of the solution is high, as carbon-fiber components can be integrated into existing production lines with minimal modifications. Furthermore, the use of carbon-fiber composites offers advantages such as improved thermal management, reduced weight, and enhanced generator efficiency, which provide long-term operational and maintenance savings. These factors make the carbon-fiber rotor carrier a viable solution for large-scale industrial applications, aligning with the renewable energy sector’s trend toward more efficient and sustainable technologies.

## VI. CONCLUSION

This paper proposed an accurate 3-D FEA loss analysis and thermal performance investigation of the ATFSPM. Based on the 3-D FEA results, losses were calculated precisely in the real-time domain, considering the temperature effect on material properties, and it has been revealed that the stray losses of the carriers are greater than the copper losses due to the high leakage flux and passivity of the rotor, which generated a huge amount of heat. Thermal modeling was carried out carefully for all components by considering the contact thermal resistance and convection heat transfer in various regions. Experimental tests confirmed the high accuracy of thermal analysis, where the maximum deviation with 3-D FEA for coils was 1.4 °C. Furthermore, by introducing the utilization of carbon-fiber instead of aluminum for the carrier material, the maximum temperature reduced by 33 °C, carrier loss decreased 99.2%, and

efficiency and power factor improved by 12.2% and 7.9%, respectively. It is evident that the proposed technique has enhanced the overall performance of the generator. The thermal analysis results ensure safe operation of the ATFSPM and support the optimal electromagnetic design.

The thermal modeling approach presented in this study, along with the innovative use of carbon-fiber rotor carriers to mitigate localized losses and overheating, is not limited to DDWTs. This technology can be adapted to a broad range of electric machines that face similar thermal challenges, particularly in high-power-density applications operating at low speeds. Such machines are commonly found in sectors like industrial motors, electric vehicles, and other renewable energy systems. The proposed approach offers an affordable and scalable solution, enabling its integration into various high-performance applications requiring effective thermal management and low-cost manufacturing.

#### REFERENCES

- [1] M. Ghods, J. Faiz, and A. A. Pourmoosa, "Winding Function Model-based Performance Evaluation of a PM Transverse Flux Generator for Applications in Direct-drive Systems," *CES Trans. on Electr. Mach. and Syst.*, vol. 8, no. 2, pp. 216–226, Jun. 2024.
- [2] Z. D. Yuan, S. F. Jia, and D. L. Liang *et al.*, "Research on Slot-pole Combination in High-power Direct-drive PM Vernier Generator for Fractional Frequency Transmission System," *CES Trans. on Electr. Mach. and Syst.*, vol. 6, no. 4, pp. 445–453, Dec. 2022.
- [3] A. Ghaheri, E. Afjei, and H. Torkaman, "Design Optimization of a Novel Linear Transverse Flux Switching Permanent Magnet Generator for Direct Drive Wave Energy Conversion," *Renewable Energy*, vol. 198, pp. 851–860, Oct. 2022.
- [4] A. Ghaheri, E. Afjei, and H. Torkaman, "A Novel Axial Air-gap Transverse Flux Switching PM Generator: Design, Simulation and Prototyping," *IET Electr. Power Appl.*, vol. 17, no. 4, pp. 452–463, Apr. 2023.
- [5] B. Lizarribar, B. Prieto, and A. Selema *et al.*, "Multiphysics Topology Optimization of Aluminium and Copper Conductors for Automotive Electrical Machines," *IEEE Trans. on Transp. Electrification*, vol. 10, no. 4, pp. 9342–9350, Dec. 2024.
- [6] S. N. Wu, Z. M. Li, and W. M. Tong, "Research on Thermal Calculation and End Winding Heat Conduction Optimization of Low Speed High Torque Permanent Magnet Synchronous Motor," *CES Trans. on Electr. Mach. and Syst.*, vol. 7, no. 4, pp. 397–403, Dec. 2023.
- [7] K. B. Tawfiq, M. Güleç, and P. Sergeant *et al.*, "A Comprehensive Study of Thermal and Performance Characteristics in Revamped Multiphase Synchronous Reluctance Machines," *IEEE Trans. on Transp. Electrification*, vol. 11, no. 1, pp. 4717–4729, Feb. 2025.
- [8] C. F. Li, Z. C. Ma, and W. Zhang *et al.*, "Realization of Tensile-bending Mechanical-thermal Coupling Fatigue based on a Uniaxial Tensile-fatigue Testing Device," *IEEE Trans. on Instrum. and Meas.*, vol. 71, pp. 1–9, Aug. 2022.
- [9] A. Zarghani, M. Farahzadi, and A. Ghaheri *et al.*, "2D Lumped Parameter Model for Temperature Prediction in a Radial Flux Switching Generator with Two Permanent Magnet Types," in *Proc. of 2023 3rd Int. Conf. on Electrical Mach. and Drives*, Tehran, Iran, Islamic Republic of, Dec. 2023, pp. 1–6.
- [10] J. K. Si, S. Z. Zhao, and H. C. Feng *et al.*, "Analysis of Temperature Field for a Surface-mounted and Interior Permanent Magnet Synchronous Motor Adopting Magnetic-thermal Coupling Method," *CES Trans. on Electr. Mach. and Syst.*, vol. 2, no. 1, pp. 166–174, Mar. 2018.
- [11] Q. X. Chen, Z. Y. Zou, and B. G. Cao, "Lumped-parameter Thermal Network Model and Experimental Research of Interior Pmsm for Electric Vehicle," *CES Trans. on Electr. Mach. and Syst.*, vol. 1, no. 4, pp. 367–374, Dec. 2017.
- [12] S. N. Wu, D. Q. Hao, and W. M. Tong, "Cooling System Design and Thermal Analysis of Modular Stator Hybrid Excitation Synchronous Motor," *CES Trans. on Electr. Mach. and Syst.*, vol. 6, no. 3, pp. 241–251, Sept. 2022.
- [13] G. J. Zhu, X. M. Liu, and L. N. Li *et al.*, "Coupled Electromagnetic-thermal-fluidic Analysis of Permanent Magnet Synchronous Machines with a Modified Model," *CES Trans. on Electr. Mach. and Syst.*, vol. 3, no. 2, pp. 204–209, Jun. 2019.
- [14] A. Zarghani, S. M. Saghin, and A. Ghaheri *et al.*, "Magneto-thermal Analysis of a Novel Excited Outer Rotor Flux-switching PM Machine," in *Proc. of 14th Power Electron., Drive Syst., and Technol. Conf.*, Babol, Iran, Islamic Republic of, Feb. 2023, pp. 1–6.
- [15] L. H. Mo, T. Zhang, and Q. Lu, "Thermal Analysis of a Flux-switching Permanent-magnet Double-rotor Machine with a 3-D Thermal Network Model," *IEEE Trans. on Appl. Supercond.*, vol. 29, no. 2, pp. 1–5, Mar. 2019.
- [16] X. H. Cai, M. Cheng, and S. Zhu *et al.*, "Thermal Modeling of Flux-switching Permanent-magnet Machines Considering Anisotropic Conductivity and Thermal Contact Resistance," *IEEE Trans. on Ind. Electron.*, vol. 63, no. 6, pp. 3355–3365, Jun. 2016.
- [17] M. Cheng, J. X. Wang, and S. Zhu *et al.*, "Loss Calculation and Thermal Analysis for Nine-phase Flux Switching Permanent Magnet Machine," *IEEE Trans. on Energy Convers.*, vol. 33, no. 4, pp. 2133–2142, Dec. 2018.
- [18] A. Zarghani, M. Farahzadi, and A. Ghaheri *et al.*, "Accurate 3D Thermal Network Development for Direct-drive Outer-rotor Hybrid-PM Flux-switching Generator," *Chin. J. of Electr. Eng.*, vol. 10, no. 2, pp. 80–92, Jun. 2024.
- [19] M. Farahzadi, K. Abbaszadeh, and S. Mirmikjoo, "Electromagnetic-thermal Analysis of a Hybrid-excited Flux Switching Permanent Magnet Generator for Wind Turbine Application," *IEEE Trans. on Energy Convers.*, vol. 38, no. 3, pp. 1962–1973, Sept. 2023.
- [20] A. Zarghani, H. Torkaman, and N. Arbab *et al.*, "Lumped Parameter Thermal Network for Thermal Analysis of a Rotor-excited Axial Flux Switching Machine with Electromagnetic-thermal Design," *Measurement*, vol. 193, pp. 110971, Apr. 2022.
- [21] J. Doering, G. Steinborn, and W. Hofmann, "Torque, Power, Losses, and Heat Calculation of a Transverse Flux Reluctance Machine with Soft Magnetic Composite Materials and Disk-shaped Rotor," *IEEE Trans. on Ind. Appl.*, vol. 51, no. 2, pp. 1494–1504, Mar.-Apr. 2015.
- [22] I. Hasan, T. Husain, and Y. Sozer *et al.*, "Mechanical and Thermal Performance of Transverse Flux Machines," in *Proc. of IEEE Energy Convers. Congr. and Expo.*, Cincinnati, OH, USA, Oct. 2017, pp. 1205–1211.
- [23] Z. Hou, J. H. Du, and Y. Wei, "Thermal Analysis of Transverse Flux Linear Switched Reluctance Motor based on Lumped Parameter Thermal Network Method," in *Proc. of 24th Int. Conf. on Electrical Machines and Systems.*, Gyeongju, Korea, Republic of, Nov. 2021, pp. 1490–1495.
- [24] G. Lei, C. C. Liu, and Y. G. Guo *et al.*, "Multidisciplinary Design Analysis and Optimization of a PM Transverse Flux Machine with Soft Magnetic Composite Core," *IEEE Trans. on Magn.*, vol. 51, no. 11, pp. 1–4, Nov. 2015.
- [25] X. Li, W. Xu, and C. Y. Ye *et al.*, "Comparative Study of Transversal-flux Permanent-magnetic Linear Oscillatory Machines for Compressor," *IEEE Trans. on Ind. Electron.*, vol. 65, no. 9, pp. 7437–7446, Sept. 2018.
- [26] R. Nasiri-Zarandi, A. Ghaheri, and K. Abbaszadeh, "Thermal Modeling and Analysis of a Novel Transverse Flux HAPM Generator for Small-scale Wind Turbine Application," *IEEE Trans. on Energy Convers.*, vol. 35, no. 1, pp. 445–453, Mar. 2020.
- [27] G. J. Zhu, Y. H. Li, and L. N. Li, "Design Optimization of a Self-circulated Hydrogen Cooling System for a PM Wind Generator based on Taguchi Method," *CES Trans. on Electr. Mach. and Syst.*, vol. 8, no. 2, pp. 170–176, Jun. 2024.
- [28] S. N. Wu, D. Q. Hao, and W. M. Tong, "Temperature Field Analysis of Mine Flameproof Outer Rotor Permanent Magnet Synchronous Motor with Different Cooling Schemes," *CES Trans. on Electr. Mach. and Syst.*, vol. 6, no. 2, pp. 162–169, Jun. 2022.
- [29] D. W. Liang, Z. Q. Zhu, and A. Dey, "High-fidelity Lumped-parameter Thermal Models for Assessing Cooling Techniques of PMSMs in EV Applications," *CES Trans. on Electr. Mach. and Syst.*, pp. 1–14, Mar.

2025.

- [30] L. N. Li, N. Jia, and X. Z. Wang *et al.*, "Cooling System Design Optimization of an Enclosed PM Traction Motor for Subway Propulsion Systems," *CES Trans. on Electr. Mach. and Syst.*, vol. 7, no. 4, pp. 390–396, Dec. 2023.
- [31] A. Infantraj, M. Augustine, and E. F. I. Raj *et al.*, "Investigation of Various Laminating Materials for Interior Permanent Magnet Brushless DC Motor for Cooling Fan Application," *CES Trans. on Electr. Mach. and Syst.*, vol. 7, no. 4, pp. 422–429, Dec. 2023.
- [32] A. Zarghani, P. Dehgoshaei, and H. Torkaman *et al.*, "Precise Loss Estimation and Comprehensive Thermal Analysis of Axial-field Flux-switching PM Machine," *Iran. J. of Electr. and Electron. Eng.*, vol. 20, no. 1, pp. 2937–2937, Mar. 2024.
- [33] A. Selema, M. N. Ibrahim, and P. Sergeant, "Additively Manufactured Ultralight Shaped-profile Windings for HF Electrical Machines and Weight-sensitive Applications," *IEEE Trans. on Transp. Electrif.*, vol. 8, no. 4, pp. 4313–4324, Dec. 2022.
- [34] B. Lizarribar, B. Prieto, and A. Selema *et al.*, "Multiphysics Topology Optimization of Aluminium and Copper Conductors for Automotive Electrical Machines," *IEEE Trans. on Transp. Electrif.*, vol. 10, no. 4, pp. 9342–9350, Dec. 2024.
- [35] A. M. Ajamloo, M. N. Ibrahim and P. Sergeant, "Design Considerations of a New IPM Rotor With Efficient Utilization of PMs Enabled by Additive Manufacturing," *IEEE Access*, vol. 12, pp. 61036–61048, Apr. 2024.
- [36] D. Staton, A. Boglietti, and A. Cavagnino, "Solving the More Difficult Aspects of Electric Motor Thermal Analysis in Small and Medium Size Industrial Induction Motors," *IEEE Trans. on Energy Convers.*, vol. 20, no. 3, pp. 620–628, Sept. 2005.
- [37] P. Dehgosha, A. Zarghani, and H. Torkaman *et al.*, "Three-dimensional Thermal Analysis of a Rotor-excited Axial Flux Switching Permanent Magnet Machine by Computational Fluid Dynamics Method," in *Proc. of 2023 3rd Int. Conf. on Electrical Mach. and Drives*, Tehran, Iran, Islamic Republic of, Dec. 2023, pp. 1–6.
- [38] R. Boutarfa, and S. Harmand, "Local Convective Heat Transfer for Laminar and Turbulent Flow in a Rotor-stator System," *Exp. in Fluids*, vol. 38, no. 2, pp. 209–221, Feb. 2005.
- [39] R. J. Wang, M. J. Kamper, and R. T. Dobson, "Development of a Thermofluid Model for Axial Field Permanent-magnet Machines," *IEEE Trans. on Energy Convers.*, vol. 20, no. 1, pp. 80–87, Mar. 2005.
- [40] D. A. Howey, A. S. Holmes, and K. R. Pullen, "Radially Resolved Measurement of Stator Heat Transfer in a Rotor-stator Disc System," *Int. J. of Heat and Mass Transf.*, vol. 53, no. 1-3, pp. 491–501, Jan. 2010.
- [41] Janna WS, *Engineering heat transfer*. CRC press, pp. 1-692, Oct. 2018.
- [42] J. F. Gieras, R. J. Wang, and M. J. Kamper, *Axial Flux Permanent Magnet Brushless Machines*. Germany: Springer Science & Business Media, pp. 1-362, Mar. 2008.
- [43] X. Ma, F. Scarpa, and H. X. Peng *et al.*, "Design of a Hybrid Carbon Fibre/carbon Nanotube Composite for Enhanced Lightning Strike Resistance," *Aerosp. Sci. and Technol.*, vol. 47, pp. 367–377, Dec. 2015.



**Aghil Ghaheri** (Member, IEEE) received the B.Sc. degree in Electrical Engineering from Shahrood University of Technology, Shahrood, Iran, in 2014, and the M.Sc. and Ph.D. degrees in Electrical Engineering from Shahid Beheshti University, Tehran, Iran, in 2016 and 2022, respectively, where he is currently working as an assistant professor at the Power Electronics and Motor Drives Laboratory. His research interests include permanent magnet and switched-reluctance machines, magnetic gears, and wireless power transfer systems. He has a

strong focus on BLDC, flux switching, transverse flux, axial field PM synchronous, flux modulated machines, coaxial magnetic gears, and PCB motors for renewable energy, automotive and household applications. His expertise is finite element analysis, analytical modelling, optimization, manufacturing, and test of electrical machines.



**Ali Zarghani** (Student Member, IEEE) was born in Mashhad, Iran, in 1997. He received a B.S. degree from the University of Birjand, Birjand, Iran, in 2018 and a M.S. degree from Shahid Beheshti University, Tehran, Iran, in 2021, both in Power Electrical Engineering. He is currently pursuing his Ph.D. with the Department of Electromechanical, Systems, and Metal Engineering, Ghent University, Ghent, Belgium. His research interests include analytical and finite element method development for multi-physics (electromagnetic, thermal, and mechanical) design, modeling, analysis, optimization, and manufacturing of various electromagnetic devices, with a focus on radial and axial flux PM machines for transportation and renewable energy applications.



**Ebrahim Afjei** (Senior Member, IEEE) received the B.S. and M.S. degrees in electrical engineering from The University of Texas at Austin, Austin, TX, USA, in 1984 and 1986, respectively, and the Ph.D. degree from New Mexico State University, Las Cruces, NM, USA, in 1991. He is currently a Professor with the Department of Electrical Engineering, Shahid Beheshti University, Tehran, Iran. His current research interests include switched reluctance motor drives and power electronics.



**Hossein Torkaman** (Senior Member, IEEE) is currently an Associate Professor with the Faculty of Electrical Engineering, Shahid Beheshti University, Tehran, Iran. He has published more than 190 technical papers in journal articles and conference proceedings, and four issued patents. He is the author of five books. He was a recipient of different awards and funds from university and companies. He is the Head of the electric machines, power electronic, and motor drives research center laboratory. His main research interests include power electronics, electrical machines, and renewable energies.